World Electric Vehicle Journal

MDPI

Article

Control of a Permanent Magnet Synchronous Motor Based on an Improved Sliding Mode Algorithm

Haiyang Xu [1], Fangbin Wang [1,*], Darong Zhu [1,2], Jiawei Ji [1,2] and Xue Gong [1,2]

[1] School of Mechanical and Electrical Engineering, Anhui Jianzhu University, Hefei 230601, China; 13865212162@163.com (H.X.); gkj@ahjzu.edu.cn (D.Z.); jijiaweei@163.com (J.J.); gongx@ahjzu.edu.cn (X.G.)
[2] Key Laboratory, Construction Machinery Fault Diagnosis and Early Warning Technology, Anhui Jianzhu University, Hefei 230601, China
* Correspondence: wangfb@ahjzu.edu.cn

Abstract

Electric forklifts depend on high-precision steering servo control to ensure handling performance and operational safety in material handling. To enhance the angle tracking accuracy and disturbance rejection of the permanent magnet synchronous motor (PMSM) in forklift steer-by-wire systems, this paper proposes an SMC algorithm based on an improved exponential reaching law. In this algorithm, the absolute value of the system state variable is introduced into the constant-rate reaching term, so that the convergence rate is dynamically adjusted through the position error and the sliding-surface parameters; a variable-boundary-layer continuous saturation function is then used instead of the sign function to provide a smooth control action. A field-oriented control (FOC) simulation model is established and compared with proportional–integral (PI) control and conventional SMC under identical conditions. The results show that the proposed algorithm delivers the fastest start-up response and the shortest rise time among the compared controllers. When a sudden load disturbance is applied, it produces only a minimal position overshoot and rapidly restores the position to the target. These findings indicate that, in both the start-up and sudden-load stages, the proposed controller provides fast response and strong disturbance rejection, thereby improving the overall motion control performance of electric forklift steering systems.

Keywords: permanent magnet synchronous motor; steer-by-wire; sliding mode control; disturbance rejection; robustness

Academic Editor: Kan Akatsu

Received: 17 October 2026
Revised: 20 November 2026
Accepted: 24 November 2026
Published: 26 November 2026

Copyright: © 2026 by the authors. Published by MDPI on behalf of the World Electric Vehicle Association. Licensee MDPI, Basel, Switzerland. This article is an open access article distributed under the terms and conditions of the Creative Commons Attribution (CC BY) license.

1. Introduction

With the rapid development of the modern logistics industry, electric forklifts have found widespread application in material handling scenarios—such as warehousing, ports, and manufacturing—thanks to advantages including environmental friendliness, energy efficiency, operational flexibility, and ease of maintenance [1]. The steering system is a core actuating system that determines a forklift's handling performance and safety. Traditional mechanical-hydraulic steering suffers from numerous limitations—such as complex architecture, sluggish response, and difficulty in integrating intelligent assistance functions—rendering it unable to meet the demands of the intelligent upgrades required for electric forklifts. Currently, electric power steering and steer-by-wire systems centered on steering motors have become the mainstream trend in the electric forklift

industry; the core of their performance lies in achieving high-precision servo control of the steering motor.

Sliding mode control, also known as sliding mode variable structure control, involves designing a switching hyperplane based on the system's desired dynamic characteristics, thereby driving the system state to converge onto the switching hyperplane from outside it. Once the system reaches the switching hyperplane, the control action ensures that it moves along the switching hyperplane to the origin. Since the system's characteristics and parameters depend solely on the designed switching hyperplane—independent of external disturbances—sliding mode variable structure control exhibits robust performance. It dynamically adapts based on the system's current state (such as the error and its derivatives), forcing the system to follow a predetermined "sliding mode" trajectory. Consequently, this control method offers advantages such as rapid response, insensitivity to parameter variations and disturbances, no requirement for online system identification, and ease of physical implementation, leading to its widespread application in the control of electric forklifts.

Theoretically, sliding mode control relies on discontinuous high-frequency switching of the control law on both sides of the sliding surface to maintain robustness. However, ideal switching characteristics cannot be achieved in the physical world; any actuator (such as an IGBT power device or the solenoid of a servo valve) exhibits time delays, dead zones, and saturation characteristics. Frequent switching action will increase the operating burden of the actuator and is not conducive to stable long-term operation of the system. Traditional sliding mode control employs a single power-law reaching law; while this offers a faster convergence rate than the exponential reaching law when the state is far from the sliding surface, the convergence rate drops to zero as the system approaches the sliding surface. In practical engineering applications, this manifests as a "creeping" phenomenon near the equilibrium point, rendering it unsuitable for the complex operating conditions of electric forklifts, and the engineering applicability of the algorithm remains to be further improved.

Zhu et al. [2] summarized the steer-by-wire control strategies for electric forklifts and identified the need for improvements in areas such as reaching law optimization, boundary layer chattering suppression, and disturbance observer-based compensation. Regarding reaching law optimization, Zhu et al. [3] proposed a non-singular terminal sliding mode controller, resolving the singularity problem associated with traditional terminal sliding mode control. Chen et al. [4] proposed a hybrid reaching law-based integral sliding mode control for position and velocity, demonstrating that the convergence time is independent of the system's initial state. Yang et al. [5] proposed a composite control strategy combining fixed-time integral terminal adaptive sliding mode control with cascaded nonlinear active disturbance rejection control. This approach employs a cascaded structure to handle high-frequency inverter dead-time effects and low-frequency load disturbances separately, while utilizing an error-adaptive sliding mode surface with an exponential term to eliminate gain singularity at the origin, thereby achieving stable speed tracking even at extremely low speeds. However, existing improvements largely target general-purpose high-speed servo applications and speed loop control, lacking specific optimization for the low-speed, high-friction operating conditions characteristic of forklifts in position servo applications. Regarding chattering suppression, Wei et al. [6] improved the traditional sliding mode control using a saturation function to reduce the speed fluctuation rate of the permanent magnet synchronous motor, and experimentally verified the effectiveness of the chattering suppression. Yu et al. [7] combined fuzzy control with non-singular terminal sliding mode control and applied the method to an in-wheel motor steering system, effectively suppressing steering chattering; however, the fuzzy rules increased the complexity of parameter tuning. More generally, fuzzy-model-based SMC

improvements exploit the nonlinear approximation capability of fuzzy rules to soften the discontinuous switching or to adapt the switching/reaching gain online, thereby reducing chattering while retaining robustness. However, their performance depends heavily on expert-defined membership functions and rule bases, which not only complicate parameter tuning and increase the computational and memory burden, but also make formal stability analysis more difficult. Such a trade-off is poorly matched to the limited processing power and the need for deterministic, maintainable software on low-cost forklift controllers. This motivates the present design, which achieves error-adaptive, smooth control through an explicit reaching law and a variable boundary layer rather than a fuzzy rule base, so that the parameters remain few and their effect and stability can be analyzed directly. To eliminate sliding mode chattering at the mechanism level, Bounasla et al. [8] introduced synergetic control into the motor drive system, inheriting the robustness of the sliding mode while eliminating chattering from the source through the continuous control law and reducing the torque ripple; Sun et al. [9] proposed a back-electromotive force (BEMF) observer based on the super-twisting algorithm; by integrating an extended state observer, they achieved simultaneous estimation of rotor states and total disturbances, effectively suppressing high-frequency chattering in BEMF estimation. However, most existing methods are designed for sensorless drive scenarios, and there is limited research on low-cost chattering suppression schemes for systems employing encoders and position loops. Traditional fixed boundary layers struggle to simultaneously ensure both accuracy and smoothness across all operating conditions; this remains a key issue hindering the practical engineering application of sliding mode control. Regarding disturbance observation and compensation, Xu et al. [10] proposed a composite control scheme combining a high-order sliding mode observer with terminal sliding mode, demonstrating effective disturbance rejection in the servo systems of construction machinery. Teng et al. [11] improved the disturbance estimation accuracy of the PMSM servo system by combining an improved disturbance observer with a super-twisting sliding mode control and optimizing the parameters using the particle swarm optimization algorithm. Wang et al. [12] proposed a variable-exponent fixed-time sliding mode fault-tolerant control strategy for a dual-motor steer-by-wire system, capable of maintaining steering tracking accuracy in the presence of actuator faults and load disturbances. In response to the bandwidth dilemma of traditional extended state observers under multi-source disturbances, Zhao et al. [13] built a new extended state observer based on a hyperlocal model, combined with simplified three-vector model predictive control to achieve parameter-independent high-precision current control, and still maintain good control performance under inductance perturbations. In addition to disturbance observers, online parameter rectification and identification represent another key route to coping with PMSM parameter variations induced by temperature drift and magnetic saturation. Zhou et al. [14] integrate parameter rectification into model predictive control to compensate for inductance and flux linkage mismatches, yet the rolling optimization and rectification modules impose high computational loads incompatible with low-cost forklift controllers. The dual-Adaline observer network method [15] achieves signal-injection-free identification of stator resistance and rotor flux linkage with high accuracy; it is complementary to the proposed sliding-mode controller, as the identified parameters can update nominal controller values in real time to further widen the robustness boundary. However, existing observer schemes primarily target sensorless applications and current-loop optimization; there is limited research addressing how to achieve velocity smoothing and disturbance compensation with minimal computational cost for the steering position loop of forklifts already equipped with encoders.

Representative schemes from the three technical routes are summarized and compared in Table 1.

Table 1. Comparison of Representative Sliding-Mode Control Schemes for PMSM Servo Systems.

Ref.	Method/Main Contribution	Target Scenario	Limitations
(a) Reaching-law and sliding-mode improvements			
[2]	Review of electric-forklift SBW strategies; identifies key improvement directions	Forklift SBW (review)	Review only; no concrete low-cost position-loop scheme
[3]	Nonsingular terminal SMC; resolves the singularity of terminal SMC	General servo drives	Not specialized for low-speed, high-friction forklift position control
[4]	Hybrid reaching-law integral SMC; convergence time independent of initial state	Position and velocity loops	Generic servo design; no forklift-specific low-speed optimization
[5]	Fixed-time integral terminal adaptive SMC with cascaded nonlinear ADRC; stable at very low speed	Speed servo; dead-time/load handling	Cascaded structure increases complexity and computational cost
(b) Chattering suppression			
[6]	Saturation function replacing the sign function; experimentally verified	PMSM speed fluctuation	Fixed boundary layer cannot balance accuracy and smoothness over the full range
[7]	Fuzzy control combined with nonsingular terminal SMC	In-wheel motor steering	Fuzzy rules increase parameter-tuning complexity
[8]	Synergetic control with a continuous control law; reduces torque ripple	Motor drive systems	Not designed for forklift position servo
[9]	Super-twisting BEMF observer integrated with an ESO	Sensorless drives	Sensorless-oriented; encoder-based position loop not addressed
(c) Disturbance observation and compensation			
[10]	High-order sliding-mode observer with terminal SMC	Construction-machinery servos	Computational cost not tailored to low-cost MCUs
[11]	Improved disturbance observer with super-twisting SMC; PSO tuning	PMSM servo; speed loop	PSO adds offline optimization burden; position loop not focused
[12]	Variable-exponent fixed-time fault-tolerant SMC	Dual-motor SBW	Dual-motor architecture raises complexity and cost
[13]	Hyperlocal-model ESO with three-vector MPC	PMSM current loop	MPC is computationally demanding; current-loop only
[14]	MPC with online parameter rectification; compensates inductance and flux linkage errors	PMSM robust drive	High computational burden; unsuitable for low-cost MCUs

[15]	Dual-Adaline observer network; injection-free identification of resistance and flux linkage	PMSM parameter monitoring	Independent perception module; not optimized for position loops
This paper	Error-adaptive reaching law arctangent variable boundary layer integral term	Encoder-based forklift position loop	Low complexity; low-cost engineering implementation

While significant progress has been made in improving the dynamic performance and engineering applicability of sliding mode control, three key limitations remain: first, existing improvements largely target high-speed servo scenarios and steer-by-wire systems for passenger cars, lacking adaptation to the specific operating conditions of forklifts—characterized by low speeds, high friction, and wide load fluctuations—where fixed-gain reaching laws struggle to balance rapid large-angle steering with smooth small-angle positioning; second, although high-order sliding mode control, cascaded observers, and predictive control offer excellent performance, their high computational demands and numerous parameters are incompatible with the limited processing power of low-cost onboard forklift controllers; third, current research focuses primarily on optimizing speed and current loops, lacking specialized solutions and low-cost engineering implementation pathways for forklift steering position servo control. Accordingly, the main contributions of this paper are summarized as follows:

1. An error-adaptive reaching law is developed by incorporating the absolute value of the position error into the constant-rate reaching term, so that the convergence rate is dynamically adjusted with the error, reconciling rapid large-angle steering with smooth small-angle positioning.
2. An arctangent-based variable boundary-layer saturation function is proposed to replace the conventional sign function; its boundary-layer thickness adapts to the error, providing a continuous, smooth control action while preserving high steady-state accuracy.
3. An integral term is introduced to eliminate the steady-state error caused by friction and backlash, yielding a simple structure that is easy to implement in engineering practice.
4. The asymptotic stability of the closed-loop system is rigorously proven via Lyapunov theory, and the effectiveness is validated through MATLAB/Simulink(R2023b) simulations (The MathWorks, Inc., Natick, MA, USA), including a CarSim (Mechanical Simulation Corporation, Ann Arbor, MI, USA) double lane-change test, providing an engineering reference for low-cost forklift steer-by-wire systems.

2. Mathematical Model of a Permanent Magnet Synchronous Motor

To accurately analyze the operating characteristics of the permanent magnet synchronous motor (PMSM) servo control system and ensure high control precision and dynamic performance, this paper adopts an idealized motor modeling approach: it assumes no magnetic saturation in the magnetic circuit and a standard sinusoidal spatial distribution of the air-gap flux linkage, and neglects hysteresis and eddy-current losses during operation. The system achieves current decoupling control of the permanent magnet synchronous motor through a $i_d = 0$ rotor flux-oriented control algorithm. Ultimately, a control effect is achieved in which the electromagnetic torque of the motor varies linearly with the stator current. The voltage equations of the PMSM in the synchronous d–q reference frame are given as [1]:

$$\begin{cases} u_d = R_s i_d + L_d \dfrac{di_d}{dt} - \omega_e L_q i_q \\ u_q = R_s i_q + L_q \dfrac{di_q}{dt} + \omega_e \left(L_d i_d + \psi_f\right) \end{cases} \tag{1}$$

The electromagnetic torque is expressed as [2]:

$$T_e = \frac{3}{2} p\left[\psi_f i_q + \left(L_d - L_q\right) i_d i_q\right] \tag{2}$$

In the equation, p is the number of pole pairs of the permanent magnet synchronous motor; i_d and i_q are the direct-axis and quadrature-axis currents in the rotating coordinate system, respectively; L_d and L_q are the direct-axis and quadrature-axis inductances, respectively; and ψ_f is the rotor permanent magnet flux linkage.

This paper focuses on a surface-mounted permanent magnet synchronous motor. Given that the stator inductances satisfy $L_d = L_q$ and the $i_d = 0$ control strategy is adopted, Equation (2) reduces to [3]:

$$T_e = \frac{3}{2} p \psi_f i_q \tag{3}$$

The mechanical equation of motion is given as [4]:

$$J \frac{d\omega_m}{dt} = T_e - T_L - B\omega_m \tag{4}$$

In the equation, J is the motor's moment of inertia; ω_m is the rotor mechanical angular velocity; T_e is the electromagnetic torque generated by the motor; T_L is the load torque acting on the shaft; and B is the mechanical damping coefficient.

Define the tracking-error state variables as [5]:

$$\begin{cases} x_1 = \theta^* - \theta \\ x_2 = \dot{x}_1 = -\dot{\theta} \\ x_3 = \dot{x}_2 = -\dot{\omega} \end{cases} \tag{5}$$

In the equation: θ^* is the desired position input to the position loop; θ is the actual rotor position.

Combining the above with the physical model of the PMSM yields:

$$\begin{cases} \dot{x}_1 = x_2 = -\omega \\ \dot{x}_2 = -\dfrac{T_e - T_L}{J} = -\dfrac{1}{J}\left[\dfrac{3}{2} P_n \psi_f i_q - T_L\right] \\ \dot{x}_3 = -\dfrac{3}{2}\dfrac{1}{J} P_n \psi_f i_q \end{cases} \tag{6}$$

Let $a = \frac{3P_n\psi_f}{2J}$, $\alpha = T_L/J$, $u_1 = i_q$, $u_2 = i_q$ then the state equation of the permanent magnet synchronous motor position servo system is

$$\begin{cases} \dot{x}_1 = x_2 \\ \dot{x}_2 = -a u_1 + F \end{cases} \tag{7}$$

Based on the aforementioned equations, the FOC scheme for the permanent magnet synchronous motor is designed as shown in Figure 1.

https://doi.org/10.3390/wevj17120624

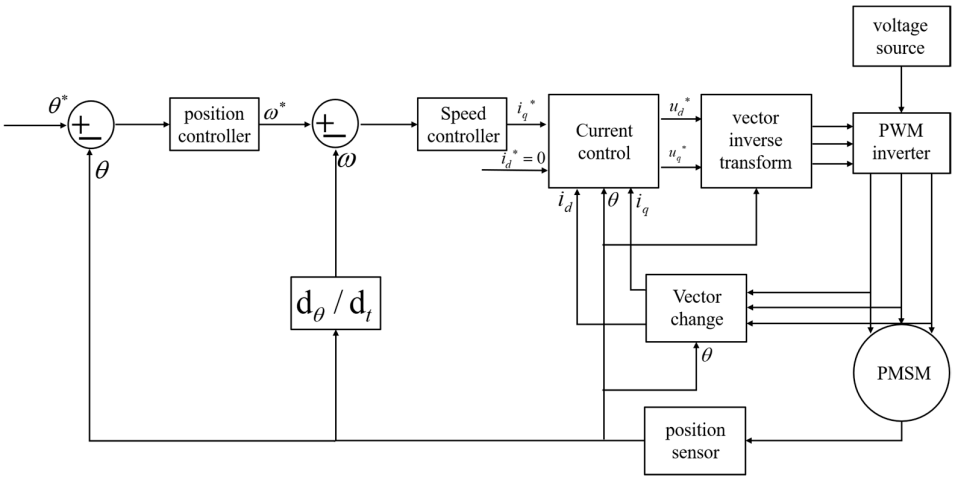

Figure 1. Block diagram of the vector control system for a permanent magnet synchronous motor (PMSM).

In the figure, the control system adopts a cascaded three-loop structure composed of a position loop, a speed loop and a current loop. The notation $d\theta/dt$ denotes the mechanical angular velocity of the rotor: it is derived by differentiating the rotor position signal acquired from the position sensor, and serves as the feedback input of the speed loop. The current and speed controllers employ conventional PI control algorithms; specifically, the q-axis reference current is determined by the output of the speed loop. The objective of this paper is to design an improved sliding-mode position controller to replace the conventional position controller in the outer loop, so as to further enhance the position tracking accuracy and disturbance rejection capability of the steering system.

3. Basic Principles of Sliding Mode Control

Sliding mode variable structure control is a unique nonlinear control technique; unlike conventional continuous control strategies, its output is discrete and discontinuous. This characteristic endows the control system with numerous excellent performance attributes, such as strong resistance to external disturbances and insensitivity to variations in system parameters, while also featuring rapid response and robust performance. Subject to the satisfaction of the constraints, the controlled system enters a sliding mode, wherein the system state undergoes small-amplitude, high-frequency reciprocating oscillations along a prescribed trajectory.

Sliding mode control is a robust nonlinear control method; its core idea is to design a sliding mode surface such that the system state slides along it after reaching it, thereby achieving the desired control objective.

Let the system state space be:

$$\dot{x} = f(x, u, t), x \in R^n, u \in R^m, t \in R \tag{8}$$

In the equation, x is the state variable of the system, and u is the control variable of the system.

The state function is defined such that $s(x) = 0$ represents the sliding mode surface; this determines the system's dynamic behavior during the sliding mode phase and simultaneously partitions the entire state space into the sliding region, the reaching region, and the leaving region. Among these, the sliding region is the area where the system maintains a sliding mode once its state enters the sliding mode surface—meaning the system moves stably along that surface. The reaching phase is the region where the system has not yet reached the sliding mode surface but is driven toward it by the control law; it

represents a transitional process during which the state gradually converges. The "departure region" refers to an area where the system state deviates from the sliding mode surface—due to factors such as system disturbances, insufficient control, or improper design—and cannot be maintained within the sliding mode dynamics; this is a state that control system designs typically aim to avoid.

When the system state is in the vicinity of the sliding mode surface, the following conditions must be satisfied:

$$\lim_{s\to 0^+} \dot{s} \le 0 \ , \lim_{s\to 0^-} \dot{s} \ge 0 \tag{9}$$

is equivalent to:

$$s \cdot \dot{s} < 0 \tag{10}$$

Consider the nonlinear system given by Equation (8); first, determine the sliding surface function $s(x) = s(x_1, x_2, x_3 \cdots x_n) = 0$. Solving for the control function at the sliding mode surface yields:

$$u(x) = \begin{cases} u^+(x) & s(x) > 0 \\ u^-(x) & s(x) < 0 \end{cases} \tag{11}$$

In the formula $u^+(x) \neq u^-(x)$, and the following conditions are satisfied:

1. The existence condition for the sliding mode must be satisfied;
2. The sliding mode reachability condition must be satisfied—that is, the sliding mode surface can be reached from any position outside it;
3. The dynamic performance of the sliding mode motion must be satisfied.

The basic structure of sliding mode control is shown in Figure 2.

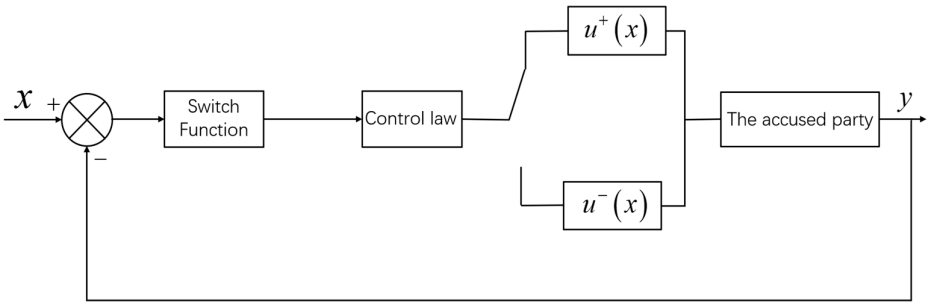

Figure 2. Schematic of the basic sliding-mode control structure, illustrating the switching function (sliding surface), the reaching-law-based control law, and the controlled plant.

In Figure 2, the design of the sliding mode variable structure controller primarily consists of two components: (1) Design the sliding mode switching function $s(x)$ By constraining the sliding mode motion through this switching function, asymptotic convergence and stability of the motion process are guaranteed, endowing the sliding mode motion with favorable dynamic characteristics. (2) Solve for the corresponding sliding mode control rates $u^+(x)$ and $u^-(x)$ to make them meet the sliding mode arrival constraint conditions. This establishes a sliding mode region on the sliding mode switching surface. By appropriately designing the sliding mode surface and control law, the system state can be driven rapidly to the sliding mode surface and made to slide along it, thereby achieving fast tracking of the target trajectory. Before the system state reaches the sliding mode surface, the controller drives it there using discontinuous switching control; once the state arrives at the surface, the system enters the sliding mode—where the state evolves in a specific manner along the surface—demonstrating significant robustness and the ability to suppress model uncertainties and external disturbances. However, in the practical context of electric forklift steering control, non-ideal factors such as switching delays (in time

and space), system inertia, measurement errors, and system "dead zones" prevent the system state from perfectly adhering to the sliding mode surface as it moves toward the equilibrium point. Instead, the state repeatedly crosses back and forth across the surface while approaching the equilibrium point, potentially preventing the system from achieving the desired control performance.

4. Improvements to the Law of Proximity

As can be seen from the basic principles, sliding mode control comprises two processes—sliding mode motion and reaching motion—as illustrated in Figure 3.

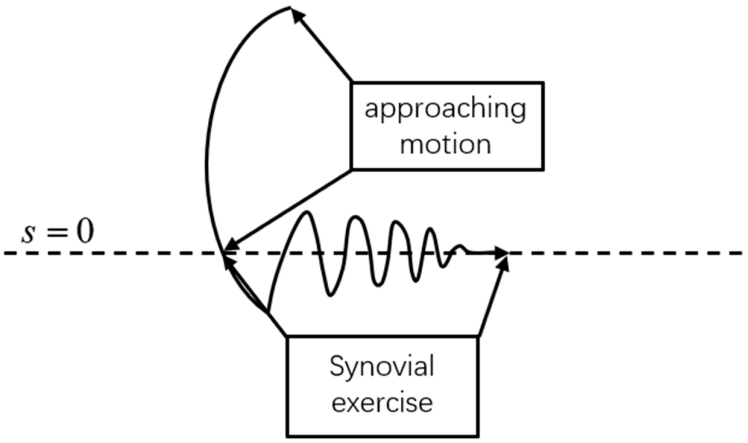

Figure 3. Phase trajectory of sliding-mode motion, showing the reaching phase (from the initial state toward the switching surface) and the sliding phase (along the switching surface to the origin).

The movement of the system from an arbitrary point toward the sliding mode surface is referred to as reaching motion, while the high-frequency oscillation occurring near the sliding mode surface is known as sliding mode motion. The reachability of the sliding mode requires that the system state—regardless of the initial conditions—reaches the predesigned sliding mode surface within a finite time; this relies on the proper design of the control law. Generally, satisfying specific Lyapunov stability conditions ensures that the system state evolves toward the sliding mode surface. However, to further enhance system performance during the reaching phase, sliding mode control employs the "reaching law" method; by designing an appropriate reaching law to regulate the speed and manner in which the system state approaches the sliding mode surface, the system's dynamic performance can be improved. Common reaching laws include the constant-rate reaching law, exponential reaching law, power-rate reaching law, and general reaching law. For the sake of discussion, this paper focuses exclusively on the exponential reaching law and proposes improvements to it.

4.1. Traditional Approaching Law Design

The traditional exponential sliding mode reaching law (ESMRL) can be expressed below, where sgn() is the signum (sign) function, which equals 1 for a positive argument, −1 for a negative argument, and 0 at zero.

$$\dot{s} = -k_1 \cdot \mathrm{sgn}(s) - k_2 s \tag{12}$$

In the equation, $k_1 \cdot \mathrm{sgn}(s)$ represents the constant-velocity reaching term, and k_1 is the switching gain; $k_2 s$ represents the exponential reaching term, and k_2 is the linear gain. For the first term $k_1 \cdot \mathrm{sgn}(s)$, the values of k_1 determine the system's convergence speed. The larger the value of k_1, the faster the system converges and the greater its

robustness; however, significant chattering occurs when the system reaches the sliding mode surface. For the second item $k_2 s$, the value of k_2 affects the initial response speed. When the system state reaches the sliding mode surface, the convergence process is asymptotic; that is, the system must reach the sliding mode surface within a finite time. When $s \neq 0$, the time required to reach the sliding mode surface can be determined by integrating Equation (12) from the initial state to the target state, with $s(0) = s_a$ and $s(t_1) = 0$.

$$t_1 = \frac{1}{k_2} \ln\left(1 + \frac{k_2}{k_1}|s_0|\right) \tag{13}$$

When the error between the initial state and the estimated state is significant, the exponential reaching law converges relatively quickly. However, this approach employs a large switching gain to compensate for system disturbances, which can lead to severe chattering and substantial deviation.

4.2. Subsection

For the control of the position segment, the spatial expression (13) is adopted, and the sliding mode surface is defined as follows:

$$s = ce_1 + e_2 \tag{14}$$

To address the aforementioned issues, the exponential reaching law is improved as follows:

$$\begin{cases} \dot{s} = -\varepsilon|e_1|\mathrm{sat}(s) - ks \\ \lim\limits_{t\to 0}|e_1| = 0 \end{cases} \tag{15}$$

In Equation (15), ε and k are both positive numbers; that is, $\varepsilon > 0$ and $k > 0$.

The aforementioned exponential reaching law modifies the constant-rate reaching term by incorporating the absolute value of the system state variable. During the initial phase of the system's approach to the sliding mode surface, the significant system error accelerates the approach process, thereby ensuring that the adjustment of the approach speed is not solely constrained by the parameters of the sliding mode surface. To balance rapid convergence with smooth control, the aforementioned reaching law employs a continuous saturation function $\mathrm{sat}(s, \delta)$ in place of the signum function $\mathrm{sgn}(s)$ used in the traditional exponential reaching law. The boundary layer of the commonly used saturation function $\mathrm{sat}(s, \delta)$ is fixed; if the boundary layer is too narrow, the benefit of the function's continuity is lost, whereas if it is too wide, the system—which would otherwise stabilize at the target point—may begin to oscillate again. Therefore, this study proposes a variable boundary-layer saturation function by utilizing the bounded nature of the arctangent function $\arctan()$ and introducing an adjustable variable β; the boundary layer is defined as follows:

$$\delta = \beta \cdot \arctan(|e_1|) \tag{16}$$

The boundary layer thickness of the saturation function is determined by $\beta \cdot \arctan(|e_1|)$, with the adjustable parameter β used to regulate the overall size of the boundary layer. When the value of $|e_1|$ is large, the system state is far from the target point; the value of the $\arctan()$ function approaches its upper limit, resulting in a thicker boundary layer and smoother system motion. Conversely, when the value of $|e_1|$ is small, the system gradually approaches the target point and the boundary layer thins out; the system tends toward ideal sliding mode control, resulting in greater stability. The saturation function equation is as follows:

$$\mathrm{sat}(s,\delta)=\begin{cases}1, & s>\beta\cdot\arctan(|e_1|)\\ \dfrac{s}{\beta\cdot\arctan(|e_1|)} & |s|<\beta\cdot\arctan(|e_1|)\\ -1, & s<-\beta\cdot\arctan(|e_1|)\end{cases} \tag{17}$$

It should be emphasized that the proposed arctangent-based variable boundary layer structure is inherently free of singularity and guarantees numerical stability throughout the full operating range.

Mathematically, the arctangent function is infinitely differentiable and continuous over the entire real number domain. When the position error approaches zero, $\arctan(|e_1|)$ is asymptotically equivalent to $|e_1|$, so the boundary layer thickness δ decreases linearly and smoothly with the error instead of collapsing abruptly to zero. Since the sliding mode variable s converges to zero synchronously with the position error, both s and δ are first-order infinitesimals near the origin, and the ratio s/δ in the saturation function remains bounded at all times, which fundamentally eliminates the division-by-zero singularity. For additional numerical robustness in digital embedded implementation, a minimum lower bound $\delta_{\min}$ can be configured in the microcontroller program as a safety threshold. It is set far below the steady-state positioning error amplitude, so it does not degrade control accuracy while providing extra stability guarantee.

The core mechanism of this design lies in the adaptive variation in the equivalent switching slope inside the boundary layer. The saturation function exhibits a linear characteristic with an effective slope of $1/\delta$: as $\delta=\beta\arctan(|e_1|)$ shrinks with the position error, the slope rises automatically to approach the ideal switching characteristic and preserve high steady-state accuracy. In this way, the slope is small for large-angle steering to maintain smooth control, and large for small-angle positioning to ensure precision, reconciling the two requirements without manual trade-off. The bounded nature of the arctangent function further prevents the boundary layer from increasing boundlessly with the error magnitude.

Although error-adaptive reaching laws and variable-boundary-layer saturation functions have been studied separately, the novelty of the proposed controller lies in their error-driven, integrated coupling rather than simple combination. Both the equivalent reaching gain in Equation (15) and the boundary layer thickness $\delta=\beta\arctan(|e_1|)$ in Equation (17) are governed by the same position error e_1: high gain and thick boundary layer accelerate convergence under large errors, while decaying gain and narrowed layer preserve steady-state accuracy as the error shrinks. Unlike the commonly used linear or exponential variable boundary layers, the arctangent-based design avoids excessive thickness at large errors and ensures numerical stability near the origin. This deterministic structure achieves fast large-angle steering and smooth small-angle positioning without fuzzy rules, online learning, or a large fixed switching gain.

To analyze the closed-loop stability, a Lyapunov function candidate is selected as [3]:

$$V=\frac{1}{2}s^2 \tag{18}$$

Based on Lyapunov stability theory, the sufficient conditions for the existence of a sliding mode surface and for the system to reach that surface in finite time are $\dot{V}=s\dot{s}\le 0$. The derivation verifying the stability of this control system is as follows:

$$\dot{V}=s\dot{s}=\ s(-\varepsilon|e_1|\mathrm{sat}(s)-ks) \tag{19}$$

$$\dot{V}=\ -\varepsilon|e_1|s\big(\mathrm{sat}(s)\big)-ks^2 \tag{20}$$

$$\dot{V} = \begin{cases} -\varepsilon|e_1||s| - ks^2, & |s| > \beta \cdot \arctan(|e_1|) \\ -\varepsilon|e_1|\dfrac{1}{\beta \cdot \arctan(|e_1|)}, & |s| < \beta \cdot \arctan(|e_1|) \end{cases} \quad (21)$$

It can be seen from Equations (12) and (13) that the parameters in Equation (21) are all positive; therefore, $\dot{V} \leq 0$. Based on the Lyapunov stability conditions, the improved exponential reaching law designed in this control algorithm ensures the system remains asymptotically stable in the presence of external disturbances.

Combining Equations (6), (15) and (21) yields the system control output equation:

$$i_q = \frac{2J}{3P_n\psi_f}\int [C\dot{e}_1 + \varepsilon|e_1|\text{sat}(s) + ks]\,dt \quad (22)$$

Let $u = i_q$ and $M = 2J/3P_n\psi_f$. Then, the mathematical model of the improved sliding-mode position controller is as follows:

$$u = M\int [C\dot{e}_1 + \varepsilon|e_1|\text{sat}(s) + ks]\,dt \quad (23)$$

In the above control law, ε, k and β are all positive constants. The parameters are selected by engineering experience combined with multiple simulation trials on the premise of satisfying the Lyapunov sliding mode reachability condition, which is a practical and widely adopted tuning method in industrial motor drive engineering.

The value selection follows unified basic principles and step-by-step procedures. First, calculate the estimated upper bound of the lumped system disturbance, including load torque fluctuation and motor parameter perturbation, according to the motor parameters and operating conditions given in Table 2. The reaching gain ε is set to 1.2–1.5 times the upper bound of the disturbance to ensure that the system state converges to the sliding surface in finite time. Second, determine the initial value of the exponential gain k according to the expected response bandwidth, and gradually increase the value under the constraint that the control output does not exceed the voltage and current saturation limits of the actuator, until the dynamic response speed meets the design requirements. Third, adjust the boundary layer coefficient β within a reasonable range to balance the steady-state positioning accuracy and control smoothness.

Table 2. Parameters of the PMSM drive system for electric steering.

Parameter Name	Numerical Value
dq-axis inductance L/mH	8.96
Stator resistance R/Ω	1.8665
Number of poles p	4
Permanent magnet flux ψ_f /Wb	0.175
Moment of inertia J/(kg. m^2)	0.003
DC bus voltage U_{dc}/V	24
Inverter current saturation threshold/A	15

All parameters adopted in this paper are tuned strictly within the physical constraints of the drive system listed in Table 1, and satisfy the sliding mode reachability condition derived from Lyapunov stability theory. Following the above three-step procedure under the same system parameters and actuator constraints, researchers can reproduce the 0.028 s step rise time reported in this paper.

Implementation within the cascaded structure. The proposed sliding-mode controller serves as the outer position controller: it replaces the proportional position controller while incorporating the speed-loop dynamics, and outputs the q-axis current reference i_q^*. The inner current loop is retained unchanged and drives the measured current i_q to

track i_q^* through field-oriented control. Hence, the current denoted by i_q in Equations (22) and (23) is the reference command rather than the measured current. Since the current loop is tuned with a bandwidth much higher than that of the position loop, the actual current follows i_q^* with negligible delay, and the designed sliding dynamics are preserved.

Since the aforementioned mathematical model of the controller incorporates an integral term, it can reduce steady-state error and enhance the system's control performance.

4.3. Digital Implementation of the Proposed Sliding Mode Controller

All continuous theoretical concepts in this paper are mapped to deterministic discrete digital signals and executable algorithms for embedded microcontrollers, and the specific operational implementation in the digital sliding mode control (DSMC) framework is described as follows.

The whole control algorithm is executed periodically in the timer interrupt service routine of the microcontroller, with a fixed sampling period $T_s = 100$ μs (10 kHz), which is consistent with the SVPWM update cycle of the inner current loop. At the beginning of each control cycle, the mechanical position signal is latched and read from the incremental encoder interface, and all state variables and control quantities are calculated sequentially.

First, the position error and speed error used to construct the sliding surface are obtained from measurable digital signals. The position error at the *k*-th sampling step is calculated as the difference between the reference position and the actual sampled position: $e_1(k) = \theta^*(k) - \theta(k)$ The speed error is obtained by the first-order backward difference in the position error, which corresponds to the differential term in the continuous sliding surface: $e_2(k) = \frac{e_1(k) - e_1(k-1)}{T_s}$ Accordingly, the discrete form of the sliding surface is: $s(k) = c \cdot e_1(k) + e_2(k)$ where c is the sliding surface bandwidth coefficient, which is configured as a fixed constant parameter and stored in the microcontroller memory after offline tuning.

Second, the error-adaptive reaching gain and the variable boundary layer saturation function are implemented as real-time algebraic operations. At each sampling step, the absolute value of the current position error $|e_1(k)|$ is substituted to calculate the equivalent reaching gain $\varepsilon \cdot |e_1(k)|$ and the boundary layer thickness $\delta(k) = \beta \cdot \arctan(|e_1(k)|)$ online. The saturation function $\mathrm{sat}\big(s(k)\big)$ is judged and calculated according to the boundary layer threshold. All operations are simple algebraic judgments and arithmetic calculations, without complex iterative operations, and are fully suitable for low-cost embedded microcontrollers.

Third, the final control output is updated in discrete form. The integral term in the control law is implemented by the Euler accumulation method, and the q-axis current reference value is updated once per control cycle and transmitted to the inner current loop as a setpoint: $i_q^*(k) = i_q^*(k-1) + \big[C\dot{e}_1(k) + \varepsilon|e_1(k)| \cdot \mathrm{sat}\big(s(k)\big) + k \cdot s(k)\big] \cdot T_s$.

All control parameters involved in the algorithm are stored as fixed constant values in the on-chip Flash after offline tuning, and no online parameter identification or iterative optimization is required during operation. The mapping from continuous mathematical definitions to discrete digital executable signals is completely clear, which supports direct transplantation and deployment on common DSP or general-purpose microcontroller platforms.

5. Simulation Verification and Analysis

To verify the performance of the aforementioned improved sliding-mode position controller, a simulation model incorporating an improved exponential reaching law was

constructed in the MATLAB/Simulink environment based on Equation (20), as shown in Figure 4.

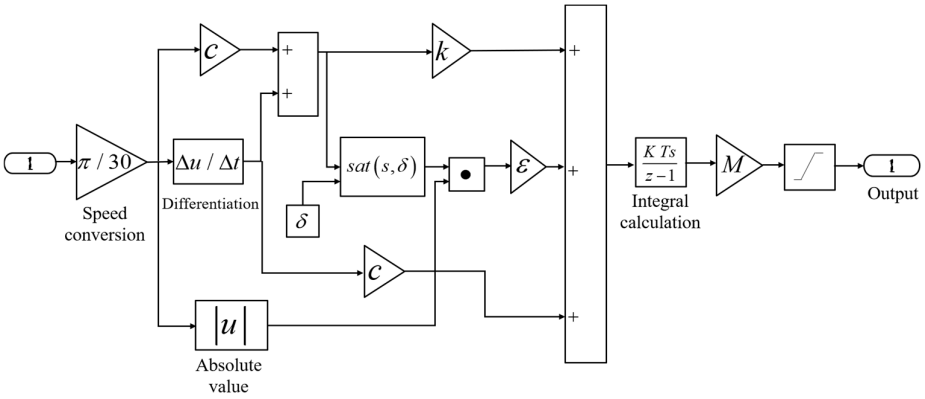

Figure 4. Simulation model of the sliding mode position controller with an improved exponential reaching law.

Given the linear relationship between the input voltage and current and the output torque and rotational speed of the permanent magnet synchronous motor (PMSM)—as well as its relatively simple mathematical model—this paper presents the parameters of the selected PMSM drive system for the forklift's electric steering system in Table 1. All motor parameters are nominal values provided by the motor manufacturer according to the product datasheet, and the voltage and current saturation parameters are consistent with the actual hardware specifications of the 24 V forklift steering drive. The drive scheme adopts Space Vector Pulse Width Modulation (SVPWM) technology.

5.1. Corner Step Simulation Analysis

To verify the dynamic response capability of the proposed controller, a step signal with a target position of 60° (mechanical angle) was applied to the system during a no-load motor startup. The position tracking curves for the three control methods are shown in Figure 5.

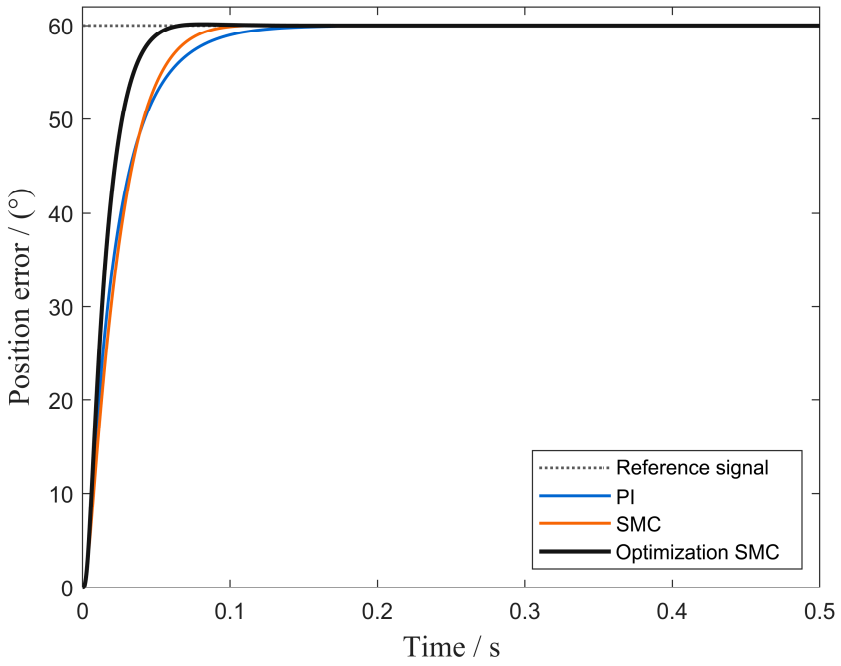

Figure 5. Position tracking responses to a 60° step reference (mechanical angle) under no-load conditions: comparison of the PI, conventional sliding-mode, and proposed improved sliding-mode controllers.

As shown in Figure 5, under the 60° step position command, the conventional SMC controller has a rise time of 0.0452 s and a settling time of 0.176 s under the ±2% steady-state error band. In contrast, the proposed optimized SMC strategy achieves a rise time of 0.028 s and a settling time of 0.149 s. Compared with the PI and conventional SMC controllers, the rise time is shortened by 44.0% and 38.1% respectively, and the settling time is reduced by 24.1% and 15.3% respectively.

The corresponding tracking errors are presented in Figure 6. It can be seen that the proposed controller exhibits a smaller peak error and faster error attenuation throughout the transient process.

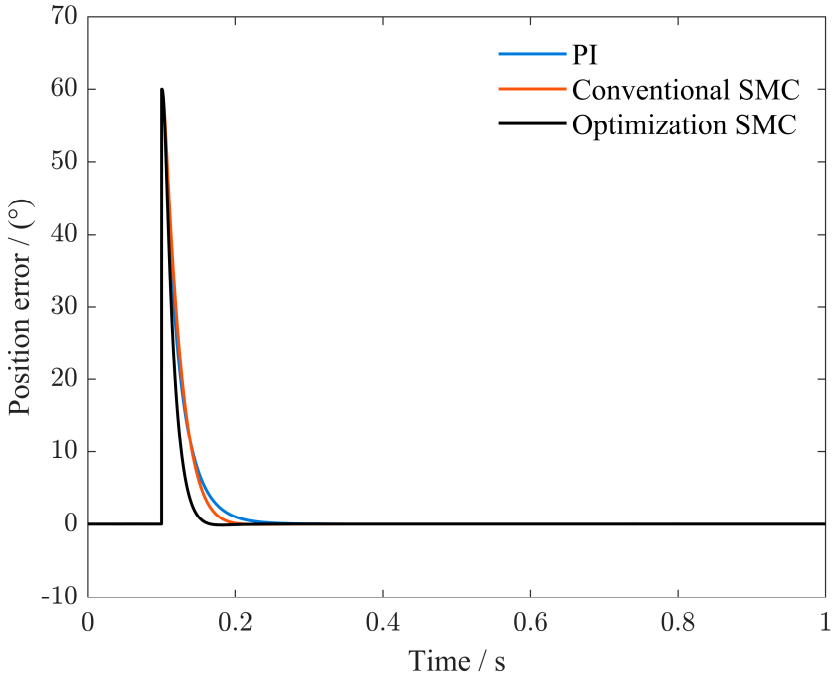

Figure 6. Position tracking errors corresponding to the 60° step responses in Figure 5 for the PI, conventional sliding-mode, and proposed controllers.

All quantitative performance indicators are calculated under unified rules to ensure the fairness and reproducibility of the comparison, and the specific definitions are as follows.

1. Rise time: Defined as the duration for the position response to rise from 10% to 90% of the steady-state target value under the step position command.
2. Settling time: Defined as the first moment when the position response enters the ±2% steady-state error band and remains within it thereafter.
3. Steady-state error: Calculated as the mean absolute value of the position tracking error over the last 20% of the total simulation time, to eliminate the influence of the transient process.
4. Integral indicators: The integral absolute error (IAE) and time-weighted integral absolute error (ITAE) are integrated over the full simulation period.
5. Disturbance recovery time: Counted from the moment when the sudden load is applied to the moment when the position error re-enters and stays within the ±2% steady-state error band.

The simulation is implemented in a discrete-time manner with a fixed sampling period of 100 μs, which is consistent with the actual execution cycle of embedded microcontrollers. All three controllers are evaluated under exactly the same reference input, load disturbance and solver settings.

To further quantify the overall tracking performance, the integral absolute error (IAE) and time-weighted integral absolute error (ITAE) are calculated over the full simulation period, as summarized in Table 3. The proposed controller achieves the lowest IAE and ITAE values among the three schemes, indicating that it delivers better comprehensive tracking accuracy in both the dynamic and steady-state stages.

Table 3. Quantitative Comparison of Comprehensive Control Performance Under Step Position Reference.

Controller	Rise Time/s	Settling Time/s	Overshoot/%	IAE/(°·s)	ITAE/(°·s²)	Steady-State Error/°	Tracking Error RMS/°
PI	0.0500	0.196	0.0018	7.49	0.484	1.63×10^{-4}	20.19
SMC	0.0452	0.176	0.0881	7.46	0.475	1.09×10^{-4}	20.30
Optimization SMC	0.0280	0.149	0.214	6.99	0.411	9.26×10^{-5}	19.93

As shown in Figure 5, the conventional SMC controller has a rise time of 0.0452 s, and the proposed optimized SMC strategy achieves a rise time of 0.028 s. Compared with the PI and conventional SMC control methods, the rise time is shortened by 44.0% and 38.1% respectively, and the dynamic response capability is significantly improved.

The corresponding tracking errors are presented in Figure 6. It can be seen that the proposed controller exhibits a smaller peak error and faster error attenuation throughout the transient process. To further quantify the overall tracking performance, the integral absolute error (IAE) and time-weighted integral absolute error (ITAE) are calculated over the full simulation period, as summarized in Table 2. The proposed controller achieves the lowest IAE and ITAE values among the three schemes, indicating that it delivers better comprehensive tracking accuracy in both the dynamic and steady-state stages.

5.2. Simulation Analysis of Double-Track Angle Following

The double lane-change maneuver is a standard test scenario for evaluating vehicle steering performance. During the test, the operator must continuously adjust the steering angle in response to the evolving driving conditions to meet specific requirements. Since the input signal for this maneuver consists of a continuously varying steering command—placing high demands on the response speed of the steering actuation system—it is also suitable for testing the tracking performance of forklift steer-by-wire systems.

In this study, a purely mechanical steering system model is constructed within the CarSim environment. To replicate real-world forklift operating scenarios, the typical operating speed for warehousing, loading/unloading, and racking tasks is set at 5 km/h. A road adhesion coefficient of 0.85 is adopted—corresponding to the adhesion characteristics of dry concrete or asphalt—representing a standard operating surface for forklifts; this choice avoids the specific disturbances associated with low-adhesion surfaces while accurately reflecting normal tire-road grip conditions.

Figure 5 illustrates the route for a typical vehicle obstacle-avoidance test—specifically, a double lane-change maneuver—which was used for this experiment. The path dimensions were determined based on the example parameters specified in the standard *GB/T 40521.1-2021: Emergency Lane-Change Test Lanes–Part 1: Double Lane-Change*; although originally developed for passenger cars, this standard is also applicable to forklifts.

The parameters in Figure 7 are $L_0 = 15\,\text{m}$, $L_1 = 5\,\text{m}$, $L_2 = 5\,\text{m}$, $L_3 = 5\,\text{m}$, $L_4 = 15\,\text{m}$, $d = 3.5\,\text{m}$ Finally, the angle signal required for pure mechanical steering is obtained as the experimental reference signal.

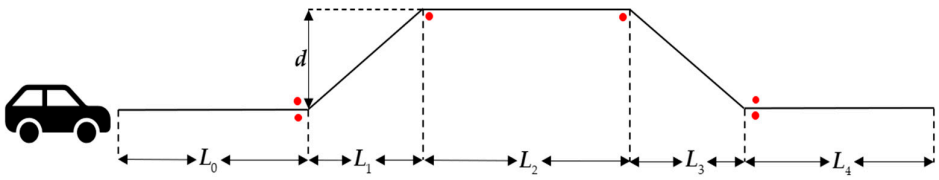

Figure 7. Route map of the double lane-change maneuver for vehicle obstacle avoidance.

During the experiment, the steering angle was recorded; during data processing, the straight-line driving segments at the beginning and end were removed, retaining only the steering signal corresponding to the intermediate angular rotation.

When the desired position follows a sinusoidal-like signal, the traditional PID controller exhibits a lag, resulting in significant tracking error, whereas the optimized SMC control algorithm demonstrates effective tracking performance. As shown by the position tracking error curves in Figures 8 and 9, the proposed optimized SMC strategy yields smaller tracking errors and higher tracking accuracy.

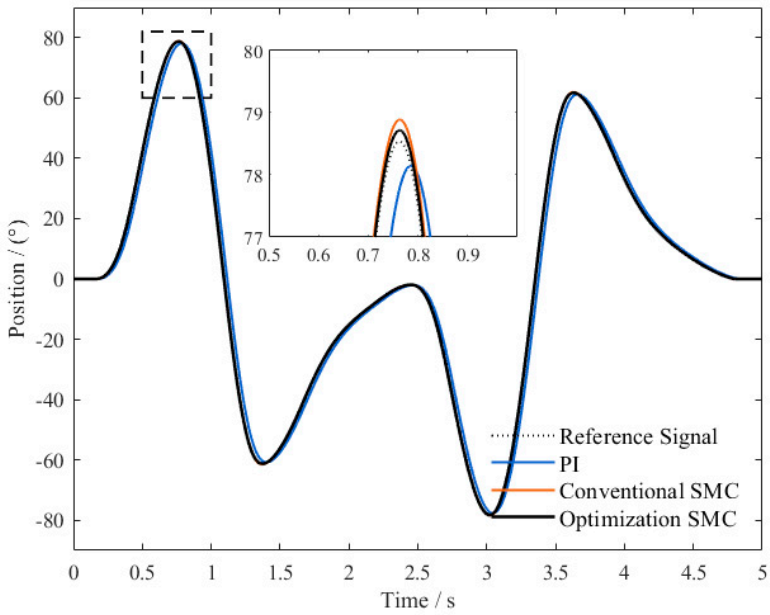

Figure 8. Position tracking responses under the double lane-change steering command (Figure 7) for the PI, conventional sliding–mode, and proposed controllers.

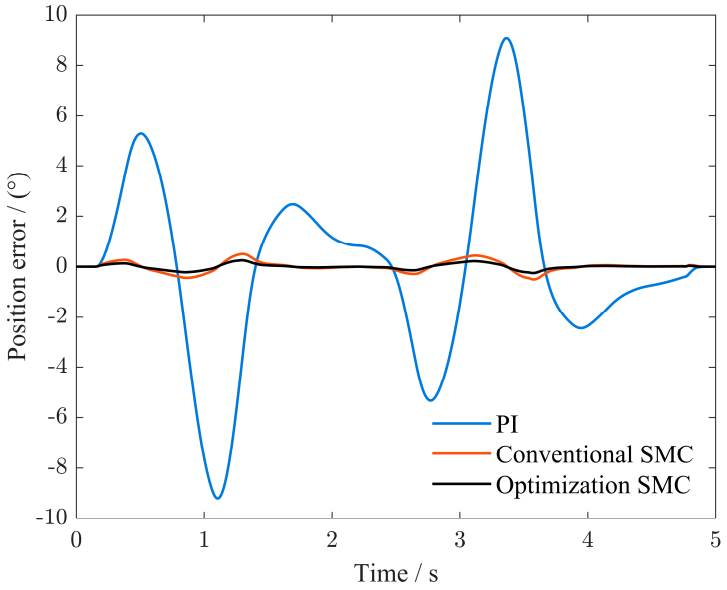

Figure 9. Position tracking errors under the double lane–change maneuver for the PI, conventional sliding-mode, and proposed controllers.

https://doi.org/10.3390/wevj17120624

5.3. Load Disturbance Analysis

To verify the capability of the proposed controller to suppress constant disturbances, a mechanical angle of 60° was set as the step command, and constant load disturbances were applied in stages during operation: a constant load of 0.1 N·m was applied at 0.5 s, followed by 0.2 N·m at 1.0 s. The position tracking curves for the three control methods are shown in Figures 10 and 11.

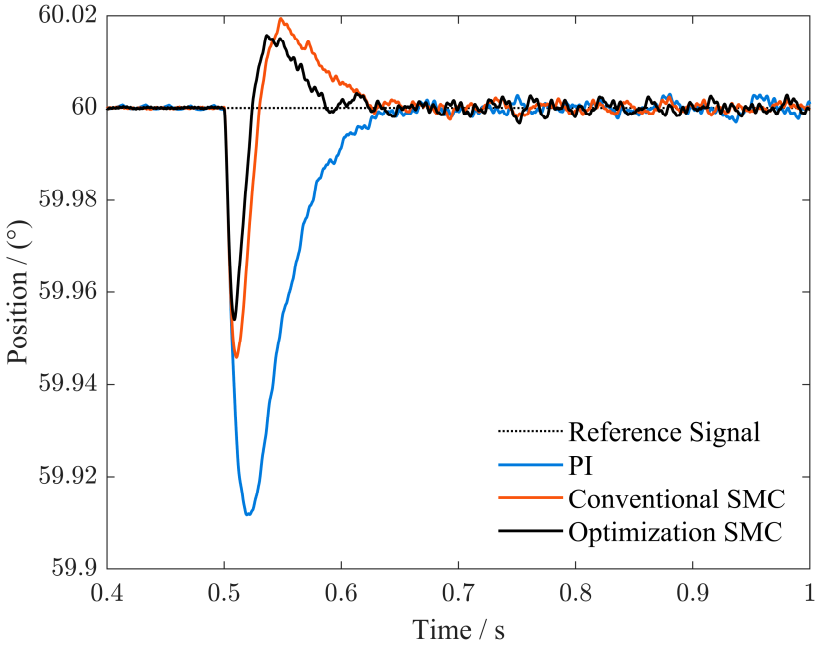

Figure 10. Position tracking curves under a constant load disturbance of 0.1 N·m.

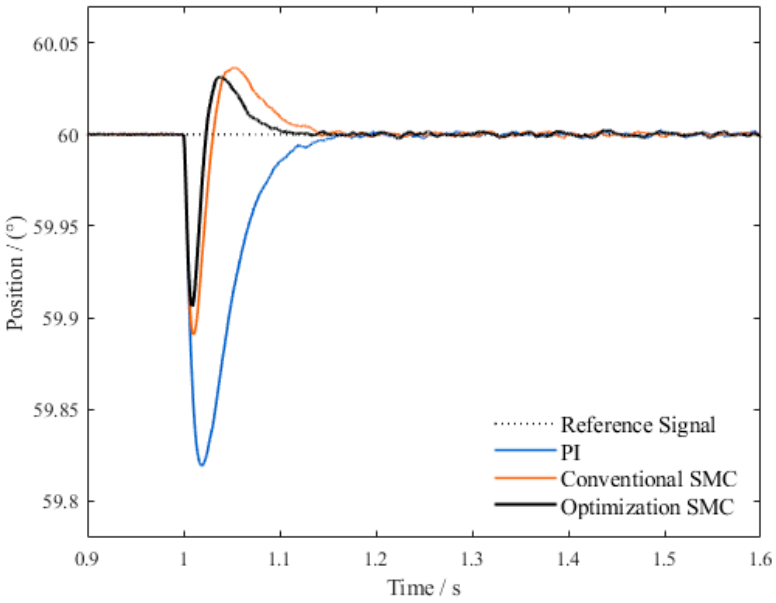

Figure 11. Position tracking curves under a constant load disturbance of 0.2 N·m.

Figure 10 shows the position tracking curves of the three controllers when a sudden load is applied at 0.5 s. It can be seen that the proposed controller exhibits the smallest speed drop and the shortest recovery time after the disturbance, confirming its stronger load rejection capability.

It can be observed that the speed signal contains noticeable high-frequency noise after load switching. This phenomenon is consistent with the actual operation characteristics of embedded digital motor control systems, and the main causes are analyzed as follows. First, the speed signal is derived by differentiating the discrete position encoder signal in digital control: the differentiation operation amplifies the position quantization noise, resulting in high-frequency burrs in the speed feedback. Second, the switching ripple generated by the SVPWM drive and the inner current loop is coupled to the mechanical output through electromagnetic torque, which further introduces small-amplitude high-frequency components in the speed response. This is an inherent characteristic of digitally driven PMSM systems rather than a defect of the control algorithm.

The peak-to-peak value of the noise is far smaller than the rated speed, so it has negligible influence on the overall dynamic response and steady-state positioning accuracy. Benefiting from the continuous saturation function and the error-adaptive gain, the proposed controller does not introduce additional high-frequency switching excitation, so the noise level remains comparable to that of the conventional SMC scheme. In practical engineering applications, the noise can be further attenuated by a first-order low-pass filter or a state observer, which will be verified in subsequent hardware prototype research.

As shown in Figures 8 and 9, traditional PID control exhibits poor disturbance rejection capabilities under constant load disturbances, resulting in significant position tracking errors. In contrast, the SMC controller and the optimized SMC controller proposed in this paper demonstrate robust disturbance rejection; the latter more effectively suppresses disturbances and accurately tracks the desired trajectory, exhibiting superior disturbance suppression and recovery capabilities.

To further verify the disturbance rejection performance of the proposed controller under abrupt shock loads, such as obstacle collision during forklift operation, a pulse impact load with an amplitude of 1 N·m and a duration of 0.1 s is applied at 1.0 s on the basis of the 60° steady-state position command. The position tracking curves of the three controllers are shown in Figure 12.

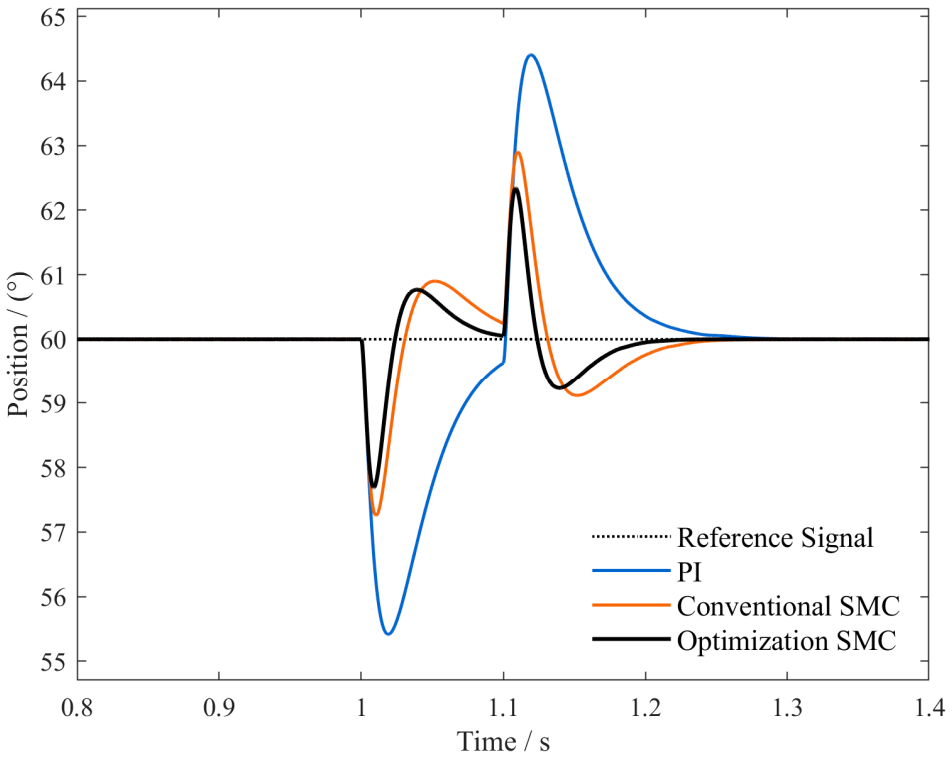

Figure 12. Position tracking curves under a pulse impact load disturbance of 1 N·m.

It can be seen from the figure that under the sudden pulse impact disturbance, all three controllers produce an instantaneous position drop. The PI controller suffers from the largest position drop and the slowest recovery speed, with an obvious lag in the disturbance attenuation process. The conventional SMC controller has a smaller drop amplitude and faster recovery, while the proposed optimized SMC controller exhibits the smallest position drop and the shortest disturbance recovery time among the three schemes.

All disturbance rejection indicators are calculated according to the unified numerical rules defined in Section 5.1, including the maximum position drop and the disturbance recovery time based on the ±2% error band criterion. The quantitative comparison results show that the proposed controller achieves the best comprehensive disturbance rejection performance among the three schemes: it effectively reduces the position deviation caused by the impact load and significantly shortens the recovery process compared with the PI and conventional SMC methods.

The results indicate that the proposed controller still maintains strong robustness and fast recovery capability under abrupt non-periodic impact loads, and is more adaptable to the complex and variable operating conditions of electric forklifts.

To verify the proposed controller's ability to suppress time-varying disturbances, a step signal with a desired position of 60° (mechanical angle) was applied. At 0.5 s, a constant load of 0.5 N·m and a sinusoidal load disturbance with a period of 1 s (i.e., $0.5\sin(2\pi t)$ N·m) were introduced. The position tracking curves of the three control methods under this condition are shown in Figure 13.

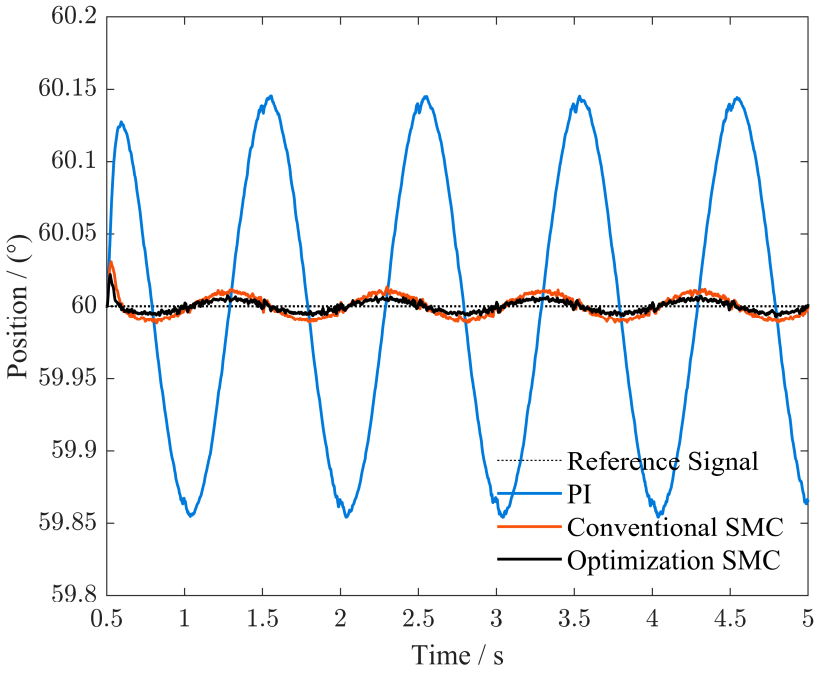

Figure 13. Position tracking curve under a sinusoidal load disturbance of 0.5 sin(2πt) N·m.

Due to the finite-time convergence characteristic of the SMC control algorithm, its disturbance rejection capability is significantly superior to that of PI control; furthermore, the improved control method achieves a tracking error of approximately ±0.05° and demonstrates robust disturbance rejection, effectively enhancing the robustness of the permanent magnet synchronous motor (PMSM) position servo system.

6. Discussion

6.1. Interpretation of Simulation Performance

The simulation results confirm that the proposed improved SMC outperforms PI control and conventional SMC in dynamic response, tracking accuracy and disturbance rejection, which can be attributed to two core design mechanisms. First, the error-adaptive reaching gain dynamically adjusts convergence speed with position error: it accelerates convergence under large-angle commands to shorten rise time, and automatically reduces gain near the equilibrium point to suppress overshoot and eliminate the "creeping" phenomenon of traditional power-law reaching laws, naturally reconciling the demand for both fast large-angle steering and smooth small-angle positioning in forklift operations. Second, the arctangent-based variable boundary layer replaces the discontinuous sign function with continuous saturation output, and its thickness adapts synchronously to error magnitude, avoiding the trade-off between steady-state accuracy and control smoothness that exists in fixed boundary layer schemes. The inherent robustness of sliding mode structure also ensures rapid recovery under load disturbances, matching the wide-load fluctuation characteristics of forklift working conditions.

6.2. Comparison with State-of-the-Art Methods

Compared with representative improved SMC schemes, the proposed method has clear differentiated positioning. Different from fuzzy-rule-based adaptive SMC, it realizes error-adaptive gain adjustment through explicit algebraic expressions without relying on expert rule bases, which reduces tuning difficulty and maintains deterministic algorithm

structure, better meeting the maintainability requirements of industrial control software. Compared with high-order sliding mode and super-twisting algorithms focusing on chattering elimination, this work does not take extreme chattering suppression as the core goal, but maintains comparable torque ripple to conventional SMC on the premise of ensuring tracking performance; its core advantage lies in extremely low computational cost, without high-order derivative operations or iterative observer calculations. Compared with composite schemes integrating disturbance observers, it copes with disturbances through the inherent robustness of sliding mode with fewer parameters and lower complexity, which is more suitable for cost-sensitive forklift steering scenarios. Overall, this work provides a practical low-cost solution complementary to existing high-performance but high-complexity schemes.

In addition, different from Model-Free Control (MFC) that completely abandons the physical system model, the proposed scheme follows the model-based sliding mode framework. MFC avoids dependence on precise model parameters and shows good adaptability to temperature-induced parameter drift, but it usually requires online lumped uncertainty estimation and is more sensitive to measurement noise. In contrast, the proposed method copes with parameter variations through the inherent robustness of sliding mode, with a simpler structure, more deterministic execution logic and lower computational cost, which is more suitable for low-cost industrial control scenarios with high reliability requirements.

6.3. Engineering Applicability for Low-Cost Forklift Controllers

For cost-sensitive forklift steer-by-wire systems, the proposed algorithm is designed to adapt to the limited computing power of low-cost on-board microcontrollers. In terms of computational complexity, all operations in a single control cycle are basic algebraic judgments, elementary function operations and Euler accumulation, with constant $O(1)$ time complexity. Compared with conventional SMC, only a small amount of elementary function calculation is added, and the overall computational burden is extremely low, which can be fully carried by common 16-bit or 32-bit general-purpose microcontrollers without high-performance DSPs. All parameters are tuned offline and stored as fixed constants, supporting direct transplantation and deployment. It should be noted that the above analysis is based on theoretical complexity evaluation at the current stage; quantitative measurement of actual execution time on target hardware will be completed in subsequent processor-in-the-loop and hardware-in-the-loop tests.

6.4. Limitations of the Current Study

The current study still has clear limitations. First, all verifications are carried out in an ideal simulation environment, and practical non-ideal factors such as inverter dead time, sensor noise, mechanical backlash and tire-ground nonlinearity are not fully incorporated. Second, parameter robustness verification only covers typical inertia variation, and extreme parameter drift conditions such as severe permanent magnet demagnetization and large-scale resistance change under high temperature have not been systematically tested. Third, the test conditions are limited to typical steering maneuvers and single-speed double lane-change cases, and more extreme operating conditions need to be further covered.

7. Conclusions

To improve the control accuracy of the steer-by-wire system of electric forklifts and enhance its robustness against load disturbances, this paper proposes an improved sliding-mode control algorithm. The absolute position error is incorporated into the reaching law so that the convergence rate is adjusted adaptively; an arctangent-based variable

boundary layer saturation function replaces the discontinuous sign function to provide a continuous, smooth control action; and an integral term is introduced to eliminate the steady-state error caused by friction and backlash. The asymptotic stability of the closed-loop system is established through a Lyapunov analysis.

Simulations were conducted first on a motor vector-control model and then on a co-simulation of the motor controller with the forklift drive system. Under identical conditions, the proposed controller was compared with a PI controller and a conventional sliding-mode controller over a 60° step command, constant and sinusoidal load disturbances (0.1 and 0.2 N·m; 0.5 sin(2πt) N·m), and a double lane-change maneuver. The results show that the proposed controller achieves a rise time of 0.028 s and a settling time of 0.149 s under the ±2% steady-state error band. Compared with the conventional SMC and PI controllers, the rise time is shortened by 38.1% and 44.0% respectively, while the settling time is reduced by 15.3% and 24.1% respectively. It also lowers the tracking error and maintains robust tracking under load disturbances, thereby improving the dynamic response and operating stability of the steering motor.

Several limitations should nevertheless be acknowledged. First, the validation is based entirely on simulations and has not been confirmed on a physical controller or a real vehicle; practical non-idealities such as inverter dead time, signal quantization, measurement noise, and computational delay are not fully represented in the simulation environment. Second, although a pulse impact load test has been supplemented to simulate abrupt non-periodic shock scenarios such as obstacle collisions, the coverage of disturbance conditions remains limited. Only a single amplitude and duration of pulse load is verified at present, and more complex random impact disturbances and continuous multi-condition shock tests have not been fully carried out. Third, the double lane-change test is limited to a single speed, and the transition from small-angle steering to sharp high-speed turns has not been fully examined. Finally, the boundary-layer and integral parameters still require manual tuning.

These limitations define the directions of future work. The algorithm will be implemented on an embedded controller and evaluated through processor-in-the-loop and hardware-in-the-loop tests, followed by real-vehicle experiments. Impulse-like shock loads and multi-speed, multi-amplitude steering maneuvers will be added to the test matrix, and the simulation model will be refined to include dead time, saturation, quantization, and discrete-time effects. In addition, automatic parameter tuning and the integration of a disturbance observer will be investigated to further improve disturbance rejection and engineering applicability. Overall, the proposed method provides a practical, low-cost reference for the motion control of forklift steer-by-wire systems under load disturbances.

Author Contributions: Conceptualization, F.W.; methodology, H.X., J.J. and D.Z.; software, H.X. and X.G.; validation, X.G. and J. Ji; investigation, H.X. and D.Z.; data curation, H.X.; writing—original draft preparation, H.X.; writing—review and editing, H.X. and F.W. All authors have read and agreed to the published version of the manuscript.

Funding: This work was supported by the China Postdoctoral Science Foundation–Anhui Joint Support Program (No. 2025T010AH), the Major Project of the Natural Science Research Project of Anhui Educational Committee (No. 2025AHGXZK30198), and the Anhui Postdoctoral Scientific Research Program Foundation (No. 2026A1273).

Data Availability Statement: The original contributions presented in this study are included in the article. Further inquiries can be directed to the corresponding author.

Conflicts of Interest: The authors declare no conflicts of interest.

References

1. Zhong, H.; Cai, Z. Discussion on design points of a heavy-duty electric forklift. *Mech. Manag. Dev.* **2025**, *40*, 112–115. (In Chinese)
2. Zhu, J.; Xing, B.; Liu, S.; Liu, H.; Xie, J.; Wang, M.; Fan, A. Review of control strategies for steer-by-wire systems. *Int. J. Automot. Technol.* **2026**. https://doi.org/10.1007/s12239-026-00518-7.
3. Zhu, Q.; Huang, X.; Zhu, Y. Non-singular terminal sliding mode control of PMSM based on new reaching law. *Mach. Tool. Hydraul.* **2022**, *50*, 148–152. (In Chinese)
4. Chen, M.; Wang, B.; Wang, G.; Qiao, Q.; Wang, Z. A novel position speed integrated sliding mode controller for PMSM servo system using new reaching law with disturbance compensation. *Electr. Eng.* **2026**, *108*, 324. https://doi.org/10.1007/s00202-026-03663-5.
5. Yang, W.; Zhang, B. Integration of cascaded nonlinear active disturbance rejection control and fixed-time integral termi-nal adaptive sliding mode control for low-speed PMSM. *J. Control. Electr. Syst.* **2026**, *37*, 1428–1448. https://doi.org/10.1007/s40313-026-01299-1.
6. Wei, Y.; Sun, L.; Chen, Z. An improved sliding mode control method to increase the speed stability of permanent magnet synchronous motors. *Energies* **2022**, *15*, 6313. https://doi.org/10.3390/en15176313.
7. Yu, X.; Fan, X.; Wang, L.; Zhao, K. Research on the electric power steering system of in-wheel motor electric vehicles based on fuzzy nonsingular terminal sliding mode control. *J. Braz. Soc. Mech. Sci. Eng.* **2026**, *48*, 257. https://doi.org/10.1007/s40430-025-06220-6.
8. Bounasla, N.; Barkat, S. Sensorless direct torque control of a five phase PMSM based on synergetic control using extended Kalman filter. *Int. J. Syst. Assur. Eng. Manag.* **2026**, *17*, 85–101. https://doi.org/10.1007/s13198-025-02926-x.
9. Sun, H.; Zhang, X.; Liu, X.; Xiong, S. Adaptive robust sensorless control for PMSM based on super-twisting algorithm back EMF observer and extended state observer. *Electr. Eng.* **2025**, *107*, 9295–9307. https://doi.org/10.1007/s00202-025-02973-4.
10. Xu, H. PMSM position servo system based on compound continuous terminal sliding mode control. *Chin. J. Constr. Mach.* **2024**, *22*, 635–640. (In Chinese)
11. Teng, R.; Zhao, X.; Jin, H.; Gao, J. Improved super-twisting sliding mode control for PMSM based on particle swarm optimization. *Electr. Eng.* **2026**, *108*, 253. https://doi.org/10.1007/s00202-026-03606-0.
12. Wang, Q.; Zhao, W.; Jiang, C. Adaptive fault-tolerant control of dual-motor SBW system for EV under actuator failures and load disturbances. *Electr. Eng.* **2026**, *108*, 159. https://doi.org/10.1007/s00202-025-03500-1.
13. Zhao, Y.; Liu, L.; Ding, S.; Ma, L. Multi-vector operated model-free predictive current control of PMSM based on a novel extended-state observer. *Int. J. Control. Syst.* **2026**, *24*, 1677–1692. https://doi.org/10.1007/s12555-026-00121-7.
14. Zhou, R.; Wang, H. Model Predictive Speed and Voltage Control of Sensorless PMSM With Parameter Rectification and A Reduced-Order EKF. *IEEE Trans. Ind. Electron.* **2026**. https://doi.org/10.1109/TIE.2026.3695118.
15. Yang, C.; Liu, W.; Song, B.; Chau, K.T. Signal-Injection-Free Online Identification of Temperature-Dependent Electrical Parameters for SPMSM Drives: An Alternating Dual-Adaline Approach. *IEEE Trans. Transp. Electrif.* **2026**, *12*, 8447–8463. https://doi.org/10.1109/TTE.2026.3696388.

Disclaimer/Publisher's Note: The statements, opinions and data contained in all publications are solely those of the individual author(s) and contributor(s) and not of MDPI and/or the editor(s). MDPI and/or the editor(s) disclaim responsibility for any injury to people or property resulting from any ideas, methods, instructions or products referred to in the content.